

www.acsanm.org Article

Thermally Stable Au-BaTiO₃ Nanoscale Hybrid Metamaterial for High-Temperature Plasmonic Applications

Di Zhang, Zhimin Qi, Jie Jian, Jijie Huang, Xin Li Phuah, Xinghang Zhang, and Haiyan Wang*



Cite This: ACS Appl. Nano Mater. 2020, 3, 1431–1437



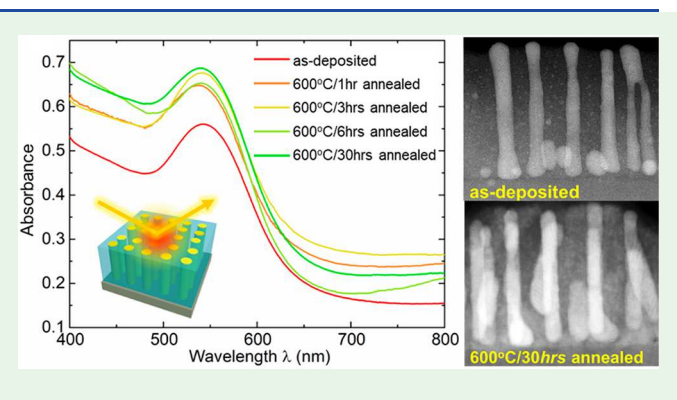
ACCESS

Metrics & More

Article Recommendations

Supporting Information

ABSTRACT: The thermal stability of the Au-BaTiO₃ nanocomposite thin film as a hybrid metamaterial deposited by a one-step pulsed laser deposition (PLD) method has been investigated via both ex situ annealing followed by TEM analysis and an in situ heating study in TEM. For the ex situ annealing study, the XRD analysis shows good crystallinity for both as-deposited and annealed films after being annealed at 600 °C for different time periods (i.e. 1, 3, 6, and 30 hours). The optical measurements including transmittance/reflectance, ellipsometry, and Raman spectroscopy demonstrate excellent optical properties of the hybrid metamaterial films by exhibiting the static localized surface plasmon resonance (LSPR) peak and hyperbolic dispersion in the visible to near-infrared regime. Both TEM results of the ex situ



annealed samples and *in situ* heating TEM results reveal no obvious microstructure change after the extensive high-temperature annealing and suggest the high thermal stability of the Au-oxide hybrid materials for their future high-temperature plasmonic applications.

KEYWORDS: thermal stability, hybrid metamaterial, ex situ, in situ, crystallinity, localized surface plasmon resonance, hyperbolic dispersion

■ INTRODUCTION

Plasmonic metamaterials are known for exhibiting novel optical properties owing to the surface plasmon polaritons (SPPs) produced from the interaction of light with metal—dielectric interfaces. The metal—dielectric hybrid metamaterials have attracted significant research interest because of the combined characteristics of two different materials resulting in pronounced differences in electromagnetic parameters. By a unique metamaterial design to manipulate SPPs and control the propagation of light within the materials, various novel optical properties can be achieved such as negative refraction, hyperbolic dispersion, cloaking, subwavelength diffraction, and nonlinear optics, which present great potentials in the fields of photovoltaics, hotocatalytics, biological and chemical sensing, land optical computing.

Recently, hyperbolic metamaterials (HMMs) have drawn much research interest. By restricting free-electron motion in one or two spatial directions, various artificial optical properties could be achieved such as hyperlens and negative refraction, which can be used to fabricate practical optical devices. Great effort has been expended to explore novel HMMs systems, and until now both layered metal—dielectric structures such as Ag/TiO₂, Ag/SiO₂, and Ag/MgF₂ and nanowire arrays with hyperbolic dispersion including Ag and Au nanowires deposited in self-assembled porous Al₂O₃

template ^{19–21} have been experimentally demonstrated. Other types of materials such as graphene ^{22,23} and highly doped semiconductors ²⁴ have also been fabricated to achieve epsilonnear-zero (ENZ) and hyperbolic media. However, most of these material systems are not stable at high temperatures, which directly restricts their lifetime and potential applications such as thermophotovoltaic conversion at high temperatures. ^{25,26} Hence, exploring thermally stable HMM systems is of significance.

Very recently, a self-assembled epitaxial Au–BaTiO₃ (BTO) vertically aligned nanocomposite (VAN) thin film was fabricated via a one-step PLD technique, showing anisotropic optical properties and ENZ in the vis–NIR regime.²⁷ The following work demonstrates highly tunable optical properties of the hybrid Au–BTO metamaterial via geometry control of the Au plasmonic phase²⁸ and its successful integration on the Si substrate with a highly tailorable optical response.²⁹ However, the thermal stability study of the typical hybrid metamaterial systems is still lacking. Considering the high

Received: November 19, 2019 Accepted: January 23, 2020 Published: January 23, 2020



thermal stability of BTO, it is believed that the Au-BTO hybrid film could possess enhanced thermal stability compared to that of pure Au films.

In this work, an *ex situ* annealing experiment and *in situ* heating in TEM were both performed to investigate the potential microstructural evolution of the Au–BTO hybrid thin film after being annealed for extended time periods under high temperatures, as the heating profiles illustrated in Figure 1. The optical property measurements including normal

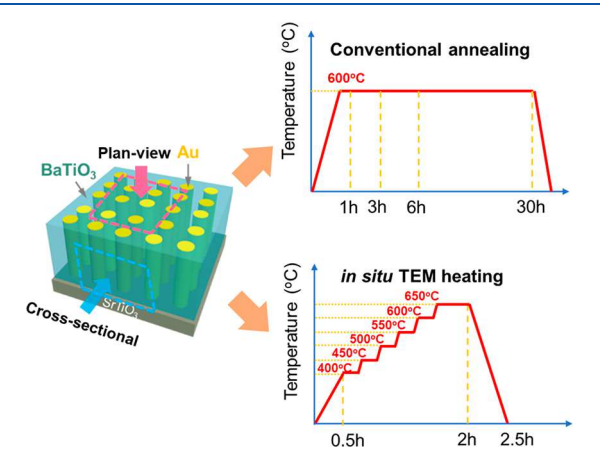


Figure 1. Schematic illustration of the Au–BaTiO₃ (Au–BTO) vertically aligned nanocomposite (VAN) thin film and heating profiles showing the conventional annealing and in situ TEM heating experiments to investigate the thermal stability of the hybrid thin film.

incident transmittance/reflectance, ellipsometry, and Raman spectroscopy were conducted to explore the optical properties of the hybrid metamaterial after thermal annealing under high temperatures for extended time periods. This thermal stability study of the oxide—metal hybrid materials also provides important information on interface stability between the oxide—metal interfaces toward future metamaterials designs for high-temperature applications.

■ EXPERIMENTAL SECTION

Thin Film Fabrication. The Au–BTO (1:1 molar ratio) composite target was prepared using a spark plasma sintering (SPS) technique. The Au–BTO thin films were deposited on single-crystalline SrTiO₃ (STO) (001) substrates using the PLD system with a KrF excimer laser (Lambda Physik Compex Pro 205, λ = 248 nm). The laser beam was focused on the target surface with an incident angle of 45° and a laser energy of about 3.0 J/cm². The distance between the target and substrate is around 4.5 cm. The deposition temperature was 600 °C, and the deposition frequency was 2 Hz. An oxygen partial pressure of 100 mTorr was maintained during the deposition. The samples were cooled at 10 °C/min under 100 mTorr O₂ pressure to room temperature after the deposition.

Microstructure Characterization. X-ray diffraction (XRD, Panalytical X'Pert X-ray diffractometer with Cu K α 1 (λ = 0.154 nm radiation source) was conducted to characterize the crystallinity of the thin film. Transmission electron microscopy (TEM) and scanning transmission electron microscopy (STEM) (in high-angle annular dark field mode (HAADF)) were taken on an FEI Talos 200X system with a point-to-point resolution of 1.6 Å. TEM samples were prepared using a standard TEM sample preparation procedure, including manual grinding, polishing, dimpling, and ion milling (PIPS 691 precision ion polishing system, Gatan Inc.). A furnace-type single-tilt in situ heating holder (model 628, Gatan Inc.) with temperature monitoring (model 1905 temperature controller, Gatan Inc.) and water recruiting systems (operates automatically when the holder temperature reaches 500 °C) was utilized in the in situ heating TEM experiment. The ramping program wasset to be 15 °C/min, and the holding time at each temperature is 10 min, as the heating profile illustrates in Figure 1. The temperature during the in situ heating TEM experiment was limited to 650 °C as a safe working temperature to avoid glue evaporation.

Optical Property Measurements. Normal incident depolarized transmittance (T%) and reflectance (R%) spectra were collected using a UV–vis–NIR absorption spectrophotometer (PerkinElmer Lambda 1050) with an integrated sphere and a total absolute measurement system (TAMS). Absorbance (A%) spectra were derived on the basis of the following optical equation: T% + R% + A% = 1. Ellipsometry measurements were conducted on a spectroscopic elliposometer (J.A. Woollam RC2) with variable angles (55, 65, and 75°) and a spectral range of 210 to 2500 nm. Two ellipsometric parameters, psi (Ψ) and delta (Δ), which are related by the equation $r_p/r_s = \tan (\Psi) e^{i\Delta}$ (where r_p and r_s are the reflection

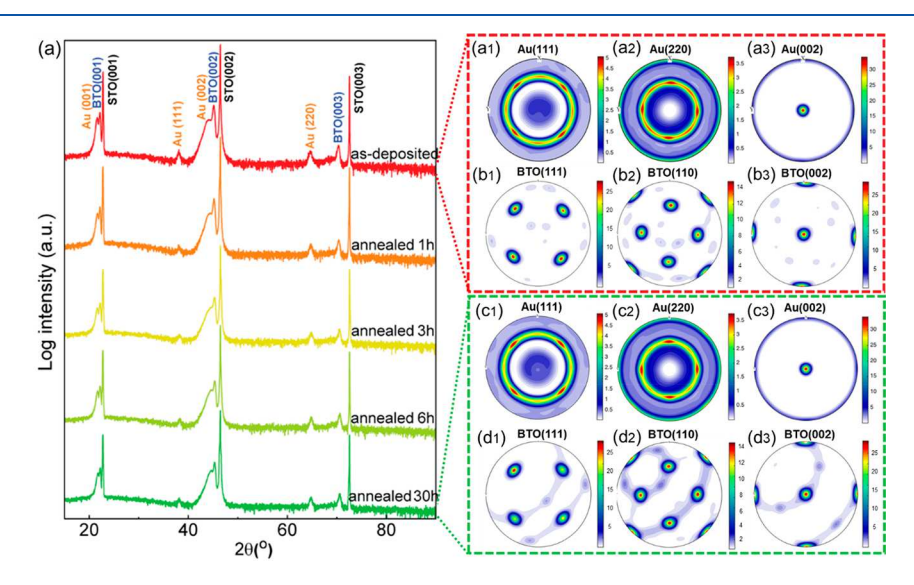


Figure 2. (a) X-ray diffraction (XRD) θ –2 θ patterns of the as-deposited and 600 °C annealed Au–BTO for different time periods (i.e., 1, 3, 6, and 30 h) for Au–BTO hybrid thin films grown on the STO (001) substrate. Pole figures of Au and BTO along poles (111), (220), and (002) for the as-deposited (a1–a3, b1–b3) and 600 °C/30 h annealed (c1–c3, d1–d3) nanocomposite films.

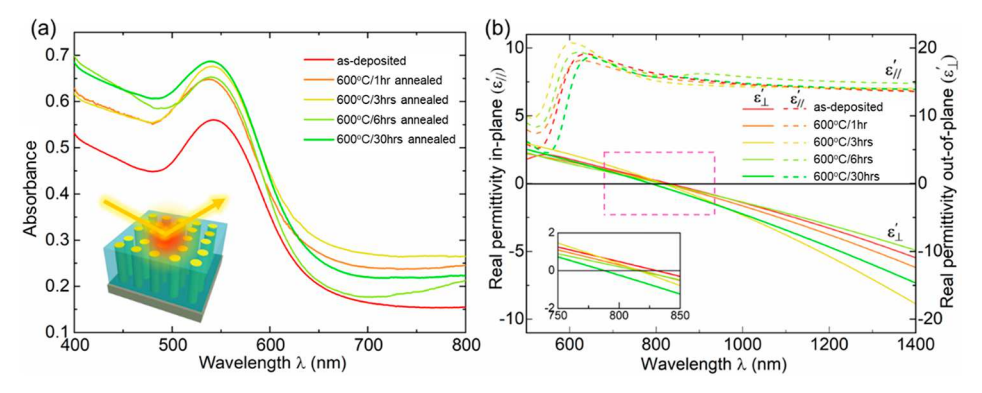


Figure 3. (a) Absorptance spectra of Au–BTO hybrid metamaterial thin films as-deposited and annealed at 600 °C for different time periods (1, 3, 6, and 30 h). (b) Real part of the in-plane $(\varepsilon'_{\parallel})$ and out-of-plane (ε'_{\perp}) permittivity of as-deposited and annealed Au–BTO thin films.

coefficients for p-polarization and s-polarization light, respectively), were obtained during the measurement. The dielectric permittivity was obtained by fitting the ellipsometric data using appropriate models in the CompleteEASE software. Here, all Au—BTO thin films were assumed to be anisotropic, thus the uniaxial model was applied. The in-plane permittivity (along the x, y direction) was modeled using Lorentz and/or Tauc-Lorentz oscillators, while the out-of-plane permittivity (along the z direction) was modeled using Lorentz and Drude oscillators due to the vertical Au nanopillar structure. A Raman spectroscopy measurement was conducted using a Raman microscope (Renishaw RM 2000) equipped with a green laser with a wavelength of 532 nm. All Raman spectra were collected by fine-focusing a $100 \times$ objective microscope, and the data acquisition time was 30 s.

RESULTS AND DISCUSSION

To identify the crystallinity of the Au-BTO hybrid thin films grown on STO (001) substrates, θ –2 θ XRD patterns of the asdeposited sample and the annealed samples at 600 °C for different annealing periods (i.e., 1, 3, 6, and 30 h) were collected and plotted in Figure 2a. For the XRD pattern of the as-deposited Au-BTO film, it shows the highly textured growth of BTO and Au along (001) orientations, with two minor extra peaks of Au(111) and Au(220). No obvious change has been observed by comparing the XRD patterns of the Au-BTO thin films after different annealing periods, indicating the high thermal stability of the nanocomposite film at 600 °C. The XRD pole figure analyses were conducted on the as-deposited and the 600 °C/30 h annealed Au-BTO films to further confirm the crystallinity and stability of the film. Figure 2a1,a3 shows the pole figures of Au(111), Au(220), and Au(002) for the as-deposited films. It is shown that Au exhibits a strong textured (002) peak, which is consistent with the above results in which the Au(002) peak is dominant. Meanwhile, Figure 2a1,a2 shows an in-plane rotation of Au(002) grains in order to minimize the lattice strain between the film and substrate. In parallel, the pole figures of BTO shown in Figure 2b1-b3 demonstrate the highly textured growth of BTO along the (00l) direction. In comparison, the pole figures of Au and BTO of the same film at 600 °C after 30 h of annealing are shown in Figure 2c1-c3,d1-d3, showing no obvious change for either Au or BTO. Overall, the pole figure analyses provide a better comparison of the crystallinity and textural properties of the Au-BTO hybrid film before and after annealing, suggesting the high thermal stability of the films.

The optical property under elevated temperature is essential for HMMs systems in future high-temperature applications. The absorbance (A%) spectra of the as-deposited and 600 °C annealed material for different time periods (1, 3,

6, and 30 h) are plotted in Figure 3a with the inset of the schematic illustration of the measurement configuration. The LSPR peaks for all curves at around 550 nm come from the plasmonic absorption of the Au phase. The transmittance (T %) spectra of all films are plotted in Figure S1, showing typical plasmonic absorption due to the LSPR of Au without an obvious peak shift. The reduction of transparency of all annealed samples is attributed to the metallic nature of the thin film after the long-time vacuum annealing.30-32 The ellipsometry data for the as-deposited and post-annealed samples were fitted to derive their dielectric permittivity values. Because of the anisotropic nature of the Au-BTO hybrid system, in-plane $(\varepsilon_{\parallel})$ and out-of-plane (ε_{\perp}) dielectric permittivity components of the films were derived by fitting ellipsometric parameter psi (Ψ) and delta (Δ) data using general oscillators to enforce the Kramers-Kronig consistency. The experimental and fitted Ψ and Δ ellipsometry data plotted in Figure S2 show a good match between the experimental and fitted data, and the very similar Ψ values in as-deposited and annealed films indicate the stable dielectric constants of the film. Figure 3b plots the real part in-plane $(\varepsilon'_{\parallel})$ and out-ofplane (ε'_{\perp}) components of permittivity of the as-deposited and annealed samples at 600 °C for different periods. It can be seen that the ε'_{\parallel} values of all films are positive throughout the wavelength range and exhibit similar features by having Au absorption peaks, while the ε'_{\perp} curves present ENZ characteristics and decrease from positive to negative at approximate 800 nm in wavelength, showing the hyperbolic dispersion in the vis-NIR wavelength regime. On the basis of the 3D symmetry of the hybrid system, there are two independent permittivity tensor components (i.e., $\varepsilon_r = \varepsilon_v = \varepsilon_{\parallel}$ and $\varepsilon_z = \varepsilon_{\perp}$). Thus, the film has one negative and two positive permittivity components (ε_z < 0, ε_x and ε_v > 0) in the near-infrared regime and belongs to type I HMMs. 15 It is noted that the hyperbolic transition wavelengths (shown as the inset in Figure 3b) of asdeposited and annealed films are very similar, except for a minor blue shift of the 600 °C/30 h annealed film due to its metallic feature as discussed previously. The imaginary part of the permittivity consisting of in-plane and out-of-plane components plotted in Figure S3 has similar features by showing the plasmonic absorption peak of Au. Furthermore, the Raman spectra of as-deposited and 600 °C/6 h and 600 °C/30 h annealed films shown in Figure S4 also have similar features, including the intensities and positions of spectra peaks. Overall, all of the optical measurement results demonstrate that the Au-BTO hybrid thin film maintains

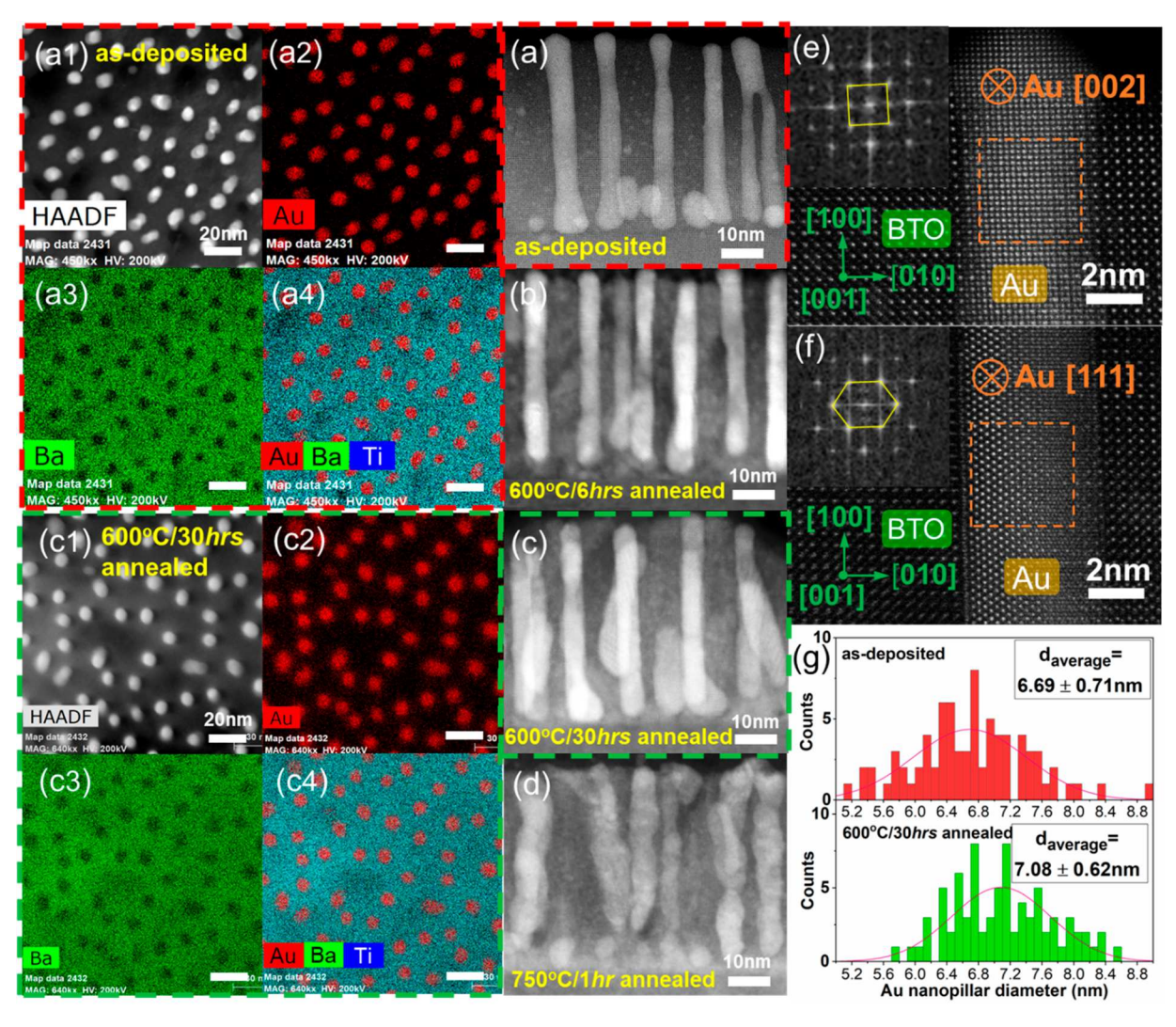


Figure 4. Cross-sectional STEM images of (a) the as-deposited and the (b) $600 \,^{\circ}\text{C}/6$ h, (c) $600 \,^{\circ}\text{C}/30$ h, and (d) $750 \,^{\circ}\text{C}/1$ h annealed Au–BTO nanocomposite thin films. Plan-view STEM images with EDS mappings of (a1–a4) as-deposited and (c1–c4) $600 \,^{\circ}\text{C}/30$ h annealed Au–BTO thin films. (e, f) HR-STEM images of the as-deposited Au–BTO thin films with the corresponding FFT patterns. (g) Statistical histogram plots of the Au nanopillar diameter distribution within the as-deposited and the $600 \,^{\circ}\text{C}/30$ h annealed Au–BTO thin films.

highly stable optical properties after being extensively annealed at 600 $^{\circ}\mathrm{C}.$

To probe the microstructure of the Au-BTO hybrid film before and after annealing, cross-section and plan-view STEM analyses were conducted on the as-deposited and 600 °C/6 h and 600 °C/30 h annealed Au-BTO thin films. Figure 4a shows the vertically aligned Au nanopillars grown throughout the BTO matrix with a film thickness of about 50 nm. Planview STEM images with EDS mappings shown in Figure 4a1a4 indicate the distinct Au and BTO phases without obvious interdiffusion. The cross-section STEM images of 600 °C/6 h and 600 °C/30 h annealed films shown in Figure 4b,c demonstrate no obvious morphological change in the Au phase after long-time annealing. The plan-view STEM and EDS results of the 600 °C/30 h annealed film illustrated in Figure 4c1-c4 show relatively blurred phase interfaces between Au nanopillars and the BTO matrix, indicating the enhanced atomic diffusion between Au and BTO under high temperatures. To further investigate the thermal stability of the Au-BTO hybrid metamaterial film at extreme temperatures, the cross-sectional STEM image and corresponding EDS results of the 750 °C/1 h annealed film are shown in Figures 4d and S5,

where the larger diameters and curved edges of Au nanopillars suggest partial melting of Au at 750 °C; another set of STEM and EDS results of the 950 °C/1 h annealed film shown in Figure S6 indicates that the Au nanopillars have partially melted and some have become Au particles embedded in a BTO matrix.

Two high-resolution STEM (HR-STEM) images taken from the as-deposited Au-BTO sample are shown in Figure 4e,f. The fast Fourier transform (FFT) patterns shown as insets demonstrate Au(002) and Au(111) growth orientations for the nanopillars, which support the XRD results. On the basis of the plan-view STEM images, the diameters of a large number (>100) of Au nanopillars in as-deposited and 600 °C/30 h annealed Au-BTO thin films are collected and shown in Figure 4g. It can be seen that the average diameter of Au nanopillars in the Au-BTO film increased from ~6.69 to ~7.08 nm after 30 h of annealing at 600 °C due to the enhanced atomic diffusion, resulting in the coarsening of Au nanopillars. The nonuniform Au nanopillar diameters lead to the broad LSPR peaks (seen in Figures 3a and S1) of the hybrid film because the plasmonic resonance wavelength is related to the size of the nanoparticles/nanopillars. 33,34

Moreover, the distribution density of Au nanopillars has been calculated on the basis of the plan-view images (Figure S7), and the average Au nanopillar spacing in as-deposited and 600 °C/30 h postannealed film samples are determined to be 20.04 and 20.14 nm, respectively, indicating no Au pillar movement or density change after long-term annealing. The constant Au nanopillar density confirms the thermal robustness of the hybrid Au-BTO film, which also explains the similar properties of as-deposited and postannealed films in the optical measurements. The selected area diffraction patterns (SADP) of the as-deposited and 600 °C/30 h annealed films taken in the [100] zone axis are shown in Figure S8, where three sets of diffraction patterns of Au in both films are indexed. On the basis of XRD, HRSTEM, and SADP analyses, the three growth-matching relations in as-deposited and 600 °C/30 h annealed films are BTO(002)//Au(002)// STO(002), BTO(002)//Au(111)//STO(002), and BTO(002)//Au(220)//STO(002).

An in situ TEM study is a powerful tool for exploring the thermal stability of nanocrystalline materials and provides an important reference for potential applications at high temperatures.³⁵ Here, to observe the real-time microstructural evolution and further clarify the thermal stability of the Au-BTO hybrid film, the in situ TEM heating experiment was performed (details in the Experimental Section). Figure 5a-f shows a series of cross-sectional STEM images of the same region in the Au-BTO film at various temperatures: asdeposited and 400, 450, 550, 600, and 650 °C. By comparing the images from as-deposited (Figure 5a) and 650 °C heated (Figure 5f) samples, no obvious morphology change has been observed, except for the minor change of one Au nanopillar, which is outlined by a yellow dashed line in both images. The minor morphology change may come from the partial melting of the Au pillar regions with large curvature (such as the top and bottom of the Au nanopillars) owing to the combined thermal excitation and e-beam effect in the TEM. Figure 5g,h shows the EDS mapping results for the as-deposited and 650 °C Au-BTO hybrid films, showing typical VAN structure and distinct Au/BTO interfaces, indicating that the film remains stable at 650 °C. Compared with other HMM material systems with low-temperature stability, the thermal robustness of the Au-BTO hybrid metamaterial is due to the unique VAN structure, where the plasmonic Au nanopillars are confined in the thermally stable BTO matrix. The reduction of diffusion length in such metal nanopillar-oxide matrix morphology leads to enhanced thermal stability of the hybrid film.

Overall, the robust thermal stability of Au-BTO hybrid metamaterials has been well demonstrated by ex situ XRD and TEM, in situ TEM heating, and optical characterizations. The localized plasmonic enhancement effect has been considered by annealing the hybrid film at high temperature for extended time periods. The thermally stable hyperbolic dispersion feature of the Au-BTO (metal-dielectric) metamaterial system makes it a great hyperbolic medium which can achieve various optical applications such as hyperbolic waveguides,³⁴ subwavelength imaging, ^{1,37} and superlenses. ^{7,38} Meanwhile, the one-step PLD technique has been proven to be a great platform for fabricating versatile hybrid metamaterials systems such as Cu-ZnO,³⁹ Au-LiNbO₃,³⁴ Co-BaZrO₃,⁴⁰ and Au-BTO-ZnO, 41 which opens up enormous possibilities in designing and processing future nanoscale hybrid metamaterials for optical, electrical, and magnetic device applications.

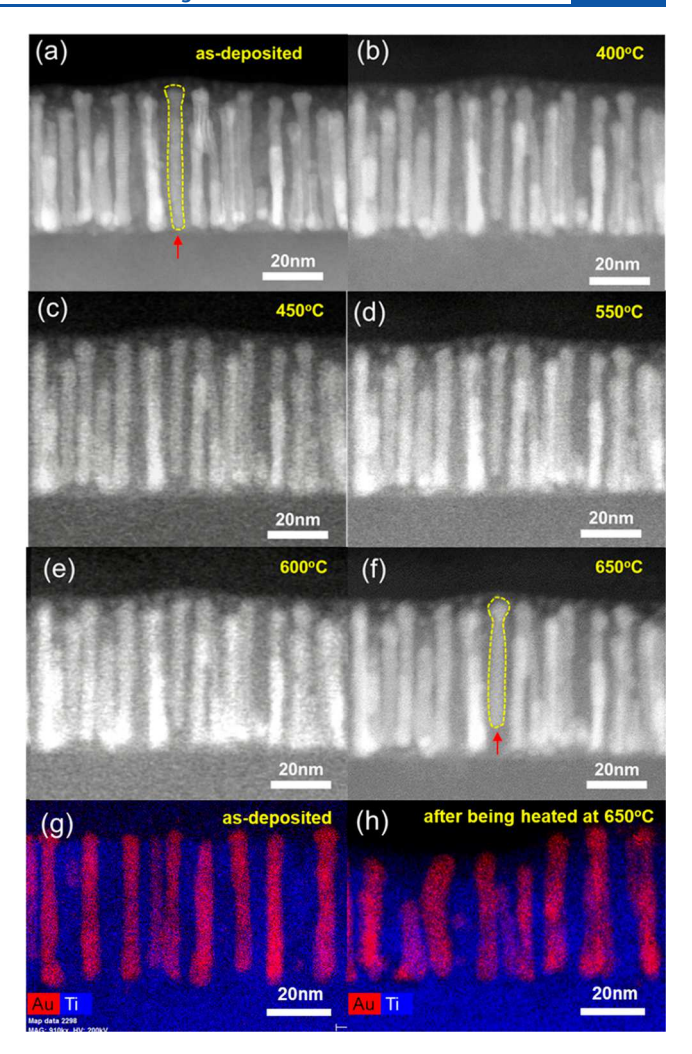


Figure 5. Cross-sectional STEM images of the Au–BTO hybrid thin film (a) as-deposited and after being heated to (b) 400, (c) 450, (d) 550, (e) 600, and (f) 650 $^{\circ}$ C during the in situ TEM heating experiment. EDS mappings of the (g) as-deposited Au–BTO thin film and (h) the 650 $^{\circ}$ C Au–BTO thin film.

CONCLUSIONS

In this work, the thermal stability of self-assembled hybrid Au–BTO hybrid thin films has been investigated. The crystallinity and microstructure of the as-deposited and annealed Au–BTO films at 600 °C were characterized by XRD, ex situ annealing, and in situ heating TEM experiments, demonstrating the excellent thermal stability of the Au–BTO film. Optical properties including absorbance, transmittance, and dielectric permittivity of the Au–BTO film remain stable at 600 °C by showing the stable LSPR absorptance peak of Au and hyperbolic dispersion in the vis–NIR regime. The thermal robustness and hyperbolic dispersion features of the Au–BTO plasmonic hybrid thin film enable it to have great potential applications for high temperature optical devices and nanophotonics.

ASSOCIATED CONTENT

Supporting Information

The Supporting Information is available free of charge at https://pubs.acs.org/doi/10.1021/acsanm.9b02271.

Transmittance spectra of as-deposited Au-BTO hybrid thin films and Au-BTO hybrid thin films annealed at 600 °C for different time periods; imaginary part dielectric permittivity; Raman spectra of as-deposited and annealed films; selected-area diffraction patterns of as-deposited and 600 °C/30 h annealed films; and cross-sectional STEM-HAADF image and EDS mappings of 750 °C/1 h and 950 °C/1 h annealed films (PDF)

AUTHOR INFORMATION

Corresponding Author

Haiyan Wang — School of Materials Engineering and School of Electrical and Computer Engineering, Purdue University, West Lafayette, Indiana 47907, United States; orcid.org/0000-0002-7397-1209; Email: hwang00@purdue.edu

Authors

- Di Zhang School of Materials Engineering, Purdue University, West Lafayette, Indiana 47907, United States
- Zhimin Qi School of Materials Engineering, Purdue University, West Lafayette, Indiana 47907, United States
- Jie Jian School of Materials Engineering, Purdue University, West Lafayette, Indiana 47907, United States
- Jijie Huang School of Materials Engineering, Purdue University, West Lafayette, Indiana 47907, United States
- Xin Li Phuah School of Materials Engineering, Purdue University, West Lafayette, Indiana 47907, United States
- **Xinghang Zhang** School of Materials Engineering, Purdue University, West Lafayette, Indiana 47907, United States

Complete contact information is available at: https://pubs.acs.org/10.1021/acsanm.9b02271

Notes

The authors declare no competing financial interest.

■ ACKNOWLEDGMENTS

This work was supported by the U.S. Department of Energy, Office of Science, Basic Energy Sciences under award DE-SC0020077. J.J. and H.W. acknowledge the support from the U.S. National Science Foundation (DMR-1809520) for high-resolution STEM/TEM work. D.Z. and X.L.P. acknowledges the support from the Office of Naval Research under contract nos. N00014-17-1-2087 and N00014-20-1-2043 for *in situ* TEM work.

REFERENCES

- (1) Barnes, W. L.; Dereux, A.; Ebbesen, T. W. Surface plasmon subwavelength optics. *Nature* **2003**, 424 (6950), 824–830.
- (2) Kuttge, M.; Vesseur, E. J. R.; Koenderink, A. F.; Lezec, H. J.; Atwarter, H. A.; de Abajo, F. G.; Polman, A. Local density of states, spectrum, and far-field interference of surface plasmon polaritons probed by cathodoluminescence. *Phys. Rev. B: Condens. Matter Mater. Phys.* **2009**, *79* (11), 113405.
- (3) Shelby, R. A.; Smith, D. R.; Schultz, S. Experimental verification of a negative index of refraction. *Science* **2001**, 292 (5514), 77–79.
- (4) Lezec, H. J.; Dionne, J. A.; Atwater, H. A. Negative refraction at visible frequencies. *Science* **2007**, *316* (5823), 430–432.
- (5) Smith, D. R.; Schurig, D. Electromagnetic wave propagation in media with indefinite permittivity and permeability tensors. *Phys. Rev. Lett.* **2003**, *90* (7), 077405.
- (6) Valentine, J.; Li, J.; Zentgraf, T.; Bartal, G.; Zhang, X. An optical cloak made of dielectrics. *Nat. Mater.* **2009**, *8* (7), 568–571.
- (7) Zhang, X.; Liu, Z. Superlenses to overcome the diffraction limit. *Nat. Mater.* **2008**, *7* (6), 435–441.

- (8) O'Brien, K.; Suchowski, H.; Rho, J.; Salandrino, A.; Kante, B.; Yin, X.; Zhang, X. Predicting nonlinear properties of metamaterials from the linear response. *Nat. Mater.* **2015**, *14* (4), 379–383.
- (9) Fan, W.; Zhang, S.; Panoiu, N. C.; Abdenour, A.; Krishna, S.; Osgood, R. M.; Malloy, K. J.; Brueck, S. R. J. Second harmonic generation from a nanopatterned isotropic nonlinear material. *Nano Lett.* **2006**, *6* (5), 1027–1030.
- (10) Clavero, C. Plasmon-induced hot-electron generation at nanoparticle/metal-oxide interfaces for photovoltaic and photocatalytic devices. *Nat. Photonics* **2014**, *8* (2), 95–103.
- (11) Kim, Y.; Smith, J. G.; Jain, P. K. Harvesting multiple electron—hole pairs generated through plasmonic excitation of Au nanoparticles. *Nat. Chem.* **2018**, *10* (7), 763–769.
- (12) Anker, J. N.; Hall, W. P.; Lyandres, O.; Shah, N. C.; Zhao, J.; Van Duyne, R. P. Biosensing with plasmonic nanosensors. In *Nanoscience and Technology: A Collection of Reviews from Nature Journals*; World Scientific. 2010, 308–319.
- (13) Kabashin, A. V.; Evans, P.; Pastkovsky, S.; Hendren, W.; Wurtz, G. A.; Atkinson, R.; Pollard, R.; Podolskiy, V. A.; Zayats, A. V. Plasmonic nanorod metamaterials for biosensing. *Nat. Mater.* **2009**, 8 (11), 867–871.
- (14) Appavoo, K.; Wang, B.; Brady, N. F.; Seo, M.; Nag, J.; Prasankumar, R. P.; Hilton, D. J.; Pantelides, S. T.; Haglund, R. F., Jr. Ultrafast phase transition via catastrophic phonon collapse driven by plasmonic hot-electron injection. *Nano Lett.* **2014**, *14* (3), 1127–1133
- (15) Poddubny, A.; Iorsh, I.; Belov, P.; Kivshar, Y. Hyperbolic metamaterials. *Nat. Photonics* **2013**, *7* (12), 948–957.
- (16) Krishnamoorthy, H. N.; Jacob, Z.; Narimanov, E.; Kretzschmar, I.; Menon, V. M. Topological transitions in metamaterials. *Science* **2012**, 336 (6078), 205–209.
- (17) Wood, B.; Pendry, J. B.; Tsai, D. P. Directed subwavelength imaging using a layered metal-dielectric system. *Phys. Rev. B: Condens. Matter Mater. Phys.* **2006**, 74 (11), 115116.
- (18) Tumkur, T. U.; Gu, L.; Kitur, J. K.; Narimanov, E. E.; Noginov, M. A. Control of absorption with hyperbolic metamaterials. *Appl. Phys. Lett.* **2012**, *100* (16), 161103.
- (19) Yao, J.; Liu, Z.; Liu, Y.; Wang, Y.; Sun, C.; Bartal, G.; Stacy, A. M.; Zhang, X. Optical negative refraction in bulk metamaterials of nanowires. *Science* **2008**, *321* (5891), 930.
- (20) Kanungo, J.; Schilling, J. Experimental determination of the principal dielectric function in silver nanowire metamaterials. *Appl. Phys. Lett.* **2010**, *97* (2), 021903.
- (21) Noginov, M. A.; Barnakov, Y. A.; Zhu, G.; Tumkur, T.; Li, H.; Narimanov, E. E. Bulk photonic metamaterial with hyperbolic dispersion. *Appl. Phys. Lett.* **2009**, *94* (15), 151105.
- (22) Iorsh, I. V.; Mukhin, I. S.; Shadrivov, I. V.; Belov, P. A.; Kivshar, Y. S. Hyperbolic metamaterials based on multilayer graphene structures. *Phys. Rev. B: Condens. Matter Mater. Phys.* **2013**, 87 (7), 075416.
- (23) Othman, M. A. K.; Guclu, C.; Capolino, F. Graphene-based tunablehyperbolic metamaterials and enhanced near-field absorption. *Opt. Express* **2013**, *21* (6), 7614–7632.
- (24) Jun, Y. C.; Reno, J.; Ribaudo, T.; Shaner, E.; Greffet, J.-J.; Vassant, S.; Marquier, F.; Sinclair, M.; Brener, I. Epsilon-near-zero strong coupling in metamaterial-semiconductorhybrid structures. *Nano Lett.* **2013**, *13* (11), 5391–5396.
- (25) Dyachenko, P. N.; Molesky, S.; Petrov, A. Y.; Stormer, M.; Krekeler, T.; Lang, S.; Ritter, M.; Jacob, Z.; Eich, M. Controlling thermal emission with refractory epsilon-near-zero metamaterials via topological transitions. *Nat. Commun.* **2016**, *7*, 11809.
- (26) Guo, Y.; Jacob, Z. Thermal hyperbolic metamaterials. *Opt. Express* **2013**, *21* (12), 15014–15019.
- (27) Li, L.; Sun, L.; Gomez-Diaz, J. S.; Hogan, N. L.; Lu, P.; Khatkhatay, F.; Zhang, W.; Jian, J.; Huang, J.; Su, Q.; Fan, M.; Jacob, C.; Li, J.; Zhang, X.; Jia, Q.; Sheldon, M.; Alù, A.; Li, X.; Wang, H. Self-assembled epitaxial Au–oxide vertically aligned nanocomposites for nanoscale metamaterials. *Nano Lett.* **2016**, *16* (6), 3936–3943.

- (28) Zhang, D.; Misra, S.; Li, L.; Wang, X.; Jian, J.; Lu, P.; Gao, X.; Sun, X.; Qi, Z.; Kalaswad, M.; Zhang, X.; Wang, H. Tunable optical properties in self-assembled oxide-metal hyrbidthin films via Au-phase geometry control: from nanopillars to nanodisks. *Adv. Opt. Mater.* **2019**, 1901359.
- (29) Kalaswad, M.; Zhang, D.; Gao, X.; Contreras, L.; Wang, H.; Wang, X.; Wang, H. Integration of hybrid plasmonic Au-BaTiO₃ metamaterial on silicon substrates. *ACS Appl. Mater. Interfaces* **2019**, 11 (48), 45199–45206.
- (30) Shim, E.; Lee, C.; Jung, E.; Lee, J.; Kim, D. S.; Lee, Y.; Kim, D. Y.; Lee, S. Enhanced native acceptor-related blue emission of ZnO thin films annealed in an oxygen ambient. *J. Korean Phys. Soc.* **2012**, 60 (11), 1939–1943.
- (31) Sendi, R. K.; Mahmud, S. Stress control in ZnO nanoparticle-based discs via high-oxygen thermal annealing at various temperatures. *J. Phys. Sci.* **2013**, 24 (1), 1–15.
- (32) Khayatian, A.; Kashi, M. A.; Azimirad, R.; Safa, S.; Akhtarian, S. A. Effect of annealing process in tuning of defects in ZnO nanorods and their application in UV photodetectors. *Optik* **2016**, *127* (11), 4675–4681.
- (33) Lee, K.-C.; Lin, S.-J.; Lin, C.-H.; Tsai, C.-S.; Lu, Y.-J. Size effect of Ag nanoparticles on surface plasmon resonance. *Surf. Coat. Technol.* **2008**, 202 (22–23), 5339–5342.
- (34) Huang, J.; Jin, T.; Misra, S.; Wang, H.; Qi, Z.; Dai, Y.; Sun, X.; Li, L.; Okkema, J.; Chen, H.-T.; Lin, P.-T.; Zhang, X.; Wang, H. Tailorable optical response of Au-LiNbO $_3$ hybrid metamaterial thin films for optical waveguide applications. *Adv. Opt. Mater.* **2018**, *6* (19), 1800510.
- (35) Zhang, C.; Fernando, J. F.; Firestein, K. L.; von Treifeldt, J. E.; Siriwardena, D.; Fang, X.; Golberg, D. Thermal stability of CsPbBr₃ perovskite as revealed by *in situ* transmission electron microscopy. *APL Mater.* **2019**, *7* (7), 071110.
- (36) He, Y.; He, S.; Yang, X. Optical field enhancement in nanoscale slot waveguidesof hyperbolic metamaterials. *Opt. Lett.* **2012**, 37 (14), 2907–2909
- (37) Yang, K. Y.; Giannini, V.; Bak, A. O.; Amrania, H.; Maier, S. A.; Phillips, C. C. Subwavelength imaging with quantum metamaterials. *Phys. Rev. B: Condens. Matter Mater. Phys.* **2012**, *86* (7), 075309.
- (38) Kawata, S.; Inouye, Y.; Verma, P. Plasmonics for near-field nano-imaging and superlensing. *Nat. Photonics* **2009**, 3 (7), 388.
- (39) Huang, J.; Wang, X.; Phuah, X. L.; Lu, P.; Qi, Z.; Wang, H. Plasmonic Cu nanostructures in ZnO as hyperbolic metamaterial thin films. *Mater. Today Nano.* **2019**, *8*, 100052.
- (40) Huang, J.; Li, L.; Lu, P.; Qi, Z.; Sun, X.; Zhang, X.; Wang, H. Self-assembled Co–BaZrO₃ nanocomposite thin films with ultra-fine vertically aligned Co nanopillars. *Nanoscale* **2017**, *9* (23), 7970–7976.
- (41) Misra, S.; Li, L.; Zhang, D.; Jian, J.; Qi, Z.; Fan, M.; Chen, H.-T.; Zhang, X.; Wang, H. Self-Assembled Ordered Three-Phase Au–BaTiO₃–ZnO Vertically Aligned Nanocomposites Achieved by a Templating Method. *Adv. Mater.* **2019**, *31* (7), 1806529.